

Southern Illinois University Edwardsville

**SPARK**

---

SIUE Faculty Research, Scholarship, and Creative Activity

---

3-31-2017

## Computational and Performance Analysis of a Continuous Magnetophoretic Bioseparation Chip with Alternating Magnetic Fields

Matin Golozar

*Southern Illinois University Edwardsville*

Majid Molki

*Southern Illinois University Edwardsville*

Jeff Darabi

*Southern Illinois University Edwardsville*

Follow this and additional works at: [https://spark.siu.edu/siue\\_fac](https://spark.siu.edu/siue_fac)



Part of the [Biomedical Devices and Instrumentation Commons](#)

---

### Recommended Citation

Golozar, M., Molki, M. & Darabi, J. *Microfluid Nanofluid* (2017) 21: 73. doi:10.1007/s10404-017-1909-4

This Article is brought to you for free and open access by SPARK. It has been accepted for inclusion in SIUE Faculty Research, Scholarship, and Creative Activity by an authorized administrator of SPARK. For more information, please contact [magrase@siue.edu](mailto:magrase@siue.edu).

# Computational and Performance Analysis of a Continuous Magnetophoretic Bioseparation Chip with Alternating Magnetic Fields

Matin Golozar · Majid Molki · Jeff Darabi

**Abstract** This paper presents the modeling and optimization of a magnetophoretic bio-separation chip for isolating cells, such as circulating tumor cells (CTCs) from the peripheral blood. The chip consists of a continuous-flow microfluidic platform that contains locally engineered magnetic field gradients. The high gradient magnetic field produced by the magnets is spatially nonuniform and gives rise to an attractive force on magnetic particles flowing through a fluidic channel. Simulations of the particle-fluid transport and the magnetic force are performed to predict the trajectories and capture lengths of the particles within the fluidic channel. The computational model takes into account key forces, such as the magnetic and fluidic forces and their effect on design parameters for an effective separation. The results show that the microfluidic device has the capability of separating various cells from their native environment. An experimental study is also conducted to verify and validate the simulation results. Finally, to improve the performance of the separation device, a parametric study is performed to investigate the effects of the magnetic bead size, cell size, number of beads per cell, and flow rate on the cell separation performance.

**Keywords** Magnetophoresis · Bioseparation chip · Particle Trajectory · Particle trapping

## 1 Introduction

Integrated microfluidic devices for magnetic cell separation is a relatively new field. Over the past decade, great progress has been made in this field and numerous microfluidic-based magnetic cell separation devices have been fabricated and tested to separate and capture various biological entities (Adams et al. 2008; Darabi and Guo 2016; Derec et al. 2010; Forbes and Forry 2012; Furlani 2007; Han et al. 2006; Hoshino et al. 2011; Jung and Han 2008; Jung et al. 2010; Khashan et al. 2014; Lee et al. 2010; Liang et al. 2013; Liu et al. 2007; Pamme and Wilhelm 2006; Plouffe et al. 2012; Shen et al. 2012; Verbarg et al. 2012; Xia et al. 2006;

---

Jeff Darabi  
Department of Mechanical Engineering, Southern Illinois University, Edwardsville, IL, USA  
E-mail: [jdarabi@siue.edu](mailto:jdarabi@siue.edu)

Zeng et al. 2013). Such microsystems typically range in size from millimeters to centimeters and are usually fabricated using polymer-based or planar glass-silicon substrates (Khashan and Furlani 2012). Implementing magnetic functionality into the microfluidic devices can be done by placing magnetic elements in the vicinity of the microchannel. Such elements produce magnetic field inside the channel which exert an attraction force on the labeled biomaterials as they flow through the channel.

The separation process requires labeling the desired biological entities with magnetic beads, which play an important role in biomedical and clinical diagnostic applications. Micrometer-sized magnetic beads are usually fabricated by encapsulating magnetite ( $Fe_3O_4$ ) nanoparticles in an organic (polymeric) or inorganic matrix (Arruebo et al. 2007). There are two common methods to bind the magnetic beads to biomaterials, direct and indirect binding. In direct binding the surface of the magnetic beads is coated with biocompatible molecules and are directly attached to the specific target biomaterial. Indirect binding requires at least one antigen to make it possible for the beads to attach to the target biomaterial (Hale and Darabi 2014).

Magnetic cell-separation technique appears to show some advantages over other methods (e.g., electric (Pethig 2010; Regtmeier et al. 2011), acoustic (Laurell et al. 2007; Lin et al. 2012), optical (Cho et al. 2010; Kayani et al. 2012), and hydrodynamic (Di Carlo 2009; Tsutsui and Ho 2009)) such as simplicity and low-cost (Liang et al. 2013). Microfluidic devices that are engineered with permanent magnets enable on-chip manipulation of magnetically labeled biomaterials which requires no power consumption. In addition, since biosample fluids usually exhibit non-magnetic properties, they are not affected by the applied magnetic field and do not interfere with the magnetically labeled materials. Additionally, magnetic cell-separation devices are less sensitive to factors such as ionic concentration, pH, and surface charge (Khashan and Furlani 2012). Another benefit of using external magnets is the prevention of sample contamination since the magnet elements are not in direct contact with the biosample fluids. The nature of continuous flow in microfluidic devices significantly reduces the amount of non-target materials that can be trapped beneath target materials and it allows for real-time monitoring of separation efficiency (Khashan and Furlani 2012; Pamme 2012).

In recent years, significant contributions have been made to the development of analytical and computational models in the field of magnetophoretic bio-separation chips. Khashan et al. (2014) performed a computational study to model a magnetic bioseparation device with flow-invasive magnetic elements to separate magnetic particles. The magnetic elements were magnetized using a bias field and placed beneath the chip with their length transverse to the flow. It was reported that the proposed scheme would overcome the limitation of the channel size and the disadvantage of short-range magnetic force. Furlani et al. (2007) proposed a microfluidic device based on a mathematical modeling for continuous separation of white and red blood cells from plasma. An external magnetic field was used to magnetize an array of integrated soft-magnetic elements that were placed transverse to the microchannel. Diamagnetic and paramagnetic behavior of WBCs and RBCs was found to be a key factor for the cell-separation process in this study. In another study, Khashan and Furlani (2012) presented a numerical approach to investigate the effects of particle-fluid coupling on particle transport and capture in a magnetic-based microfluidic device. Their analysis showed that at high

particle concentrations, a one-way particle-fluid coupling (assuming that the particles do not affect the fluid flow) overpredicted the magnetic force required to capture the particles. The authors concluded that for more accurate predictions, two-way particle-fluid coupling was required. Kashevsky et al. (2013) presented an analytical model to study the motion of superparamagnetic particles driven by a non-uniform magnetic field in a liquid. The model can be used to analyze and design batch systems with different shapes of magnets.

The work presented in this paper combines magnetic fields, fluid fields, and particle tracing to simulate the trajectories of tens of thousands of particles in a microfluidic platform. This microfluidic-based magnetophoretic bioseparation chip utilizes locally engineered high magnetic field gradients and offers significantly higher throughputs compared to the recently developed microfluidic devices where flow rates were limited to less than 30 mL/h (Chen et al. 2014; Earhart et al. 2014). In addition, this study presents a comprehensive parametric study to optimize the performance of the bioseparation chip

## 2 Theoretical background

Figure 1 shows a schematic representation of the magnetic separation chip. A mixture of target and non-target cells, is introduced into the separation channel. Among the particles moving along the channel, those with beads attached to them experience a magnetic force, which is governed by the gradient of the magnetic flux, and are pulled downward and immobilized on the magnetic surfaces. As the particles move forward, the target cells are trapped by the magnetic field and the non-target cells that are not affected by the magnetic field will flow out through the separation channel.

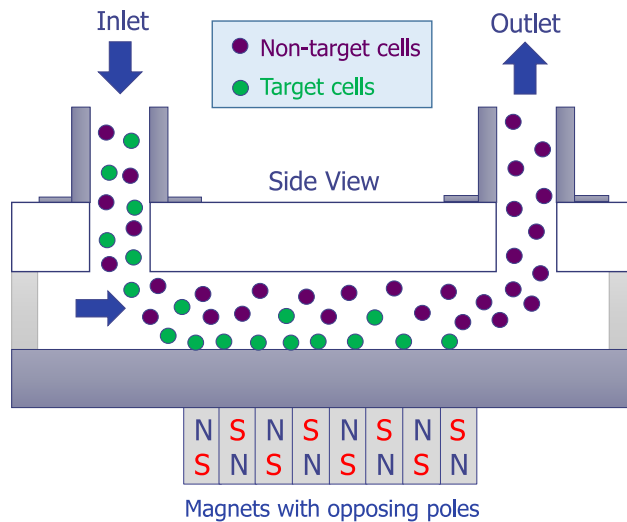


**Fig. 1** Schematic of the magnetic cell separation device.

In the presence of an external magnetic field, the dominant forces acting on a magnetic particle traveling through a magnetophoretic chip are the hydrodynamic drag force ( $F_d$ ), the gravitational force ( $F_g$ ), and the magnetic force ( $F_m$ ) (Inglis et al. 2004). The magnetic force exerts an attractive force on magnetically-labeled particles and selectively pulls them towards the permanent magnets. In general, the magnetic force acting on a magnetic particle can be written as (Purcell and Morin 2013)

$$\mathbf{F}_m = (\mathbf{m}_b \cdot \nabla)\mathbf{B} \quad (1)$$

where  $m_b$  is the magnetic dipole moment of the particle and  $B$  is the applied magnetic field (Bleaney and Bleaney 1989; Jackson 1999). If the particle has a volumetric magnetization  $M_b$ , the dipole moment of the particle is given by (Purcell and Morin 2013)

$$\mathbf{m}_b = V_b \mathbf{M}_b \quad (2)$$

where  $V_b$  is the volume of the magnetic bead. The magnetic beads used in this study show superparamagnetic behavior. Superparamagnetic beads are soft magnetic materials and do not retain their magnetism after applied magnetic field is removed. The magnetization of the bead is a function of the applied magnetic field and is a linear function of the field intensity up to a magnetic flux of approximately 0.1 T, after which it remains nearly constant, with a saturation magnetization of  $M_{sat}$  that is independent of the applied magnetic field (Darabi and Guo 2013). In the saturation region, which is the case in this study, the magnetization is nearly constant,  $M_b = M_s$ , and the magnetic force can be approximated as

$$\mathbf{F}_m = V_b (\mathbf{M}_{sat} \cdot \nabla)\mathbf{B} \quad (3)$$

In order to implement an effective separation, magnetic beads must be attached to the cell surface. The resulting cell-bead complex is not spherical, which makes it difficult to calculate the drag force. However, if the bead size is small compared to the cell size, the approach presented by Häfeli et al. (Häfeli et al. 2013) can be used to estimate the drag force. If  $N$  magnetic beads bind to a cell, the effective mass, volume, density, and radius of the cell-bead structure can be estimated by

$$m_p = m_c + N m_b = \rho_c V_c + N \rho_b V_b \quad (4)$$

$$V_p = V_c + N V_b \quad (5)$$

$$\rho_p = \frac{\rho_c V_c + N \rho_b V_b}{V_c + N V_b} \quad (6)$$

$$R_p = \left(\frac{3}{4\pi} V_p\right)^{1/3} \quad (7)$$

where  $N$  is the number of magnetic beads and subscripts p, c, and b represent cell-bead complex, cell, and bead, respectively. Since the magnetic beads used in this study are much smaller compared to the cells they are attached to (1 micron

beads vs. 10 to 30 micron cells), the use of effective radius in drag force calculation does not introduce a significant error. Assuming that magnetically labeled cells are spherical, the hydrodynamic drag force is described by Stokes' law.

$$\mathbf{F}_d = 6\pi\eta R_p(\mathbf{V}_p - \mathbf{V}_f) \quad (8)$$

where  $R_p$  is the radius of the cell-bead structure,  $\eta$  is the fluid viscosity, and  $\mathbf{V}_p$  and  $\mathbf{V}_f$  are the velocities of the particle and fluid, respectively.

The net gravitational force, which can be defined as the difference between the weight of an immersed particle and an upward buoyancy force exerted by fluid, is given by

$$\mathbf{F}_g = -V_p(\rho_p - \rho_f)\mathbf{g} \quad (9)$$

where  $V_p$ ,  $\rho_p$ ,  $\rho_f$ , and  $\mathbf{g}$  are the particle volume, the density of the particle and fluid, and the acceleration due to gravity, respectively. It is also worth mentioning that, particle-particle interaction and particle-fluid interaction can be ignored for particle suspensions with small particle volume concentration of less than 5%, which is the case in the present study (Furlani 2006).

### 3 Device physics and design

Figure 2 shows an image of the assembled microfluidic chip. The device consists of a continuous-flow microfluidic chip that contains high gradient magnetic fields along the channel. High gradient magnetic fields, produced by an array of magnets with opposing poles are spatially non-uniform and provide large attractive forces on magnetic particles that travel through the channel. The chip is made of a bottom glass substrate, inlet outlet ports, a buffer port, a thin double-sided polyimide tape in which the separation channel is made, and a top coverslip. A microscope slide with dimensions of 25 mm  $\times$  75 mm  $\times$  1 mm is used as the bottom glass substrate. The top substrate is a glass coverslip with the same dimensions, but a thinner thickness of 160  $\mu\text{m}$ . This thin coverslip made it possible to view the 1  $\mu\text{m}$  magnetic particles at high magnifications. Three 1 mm holes were drilled in the top substrate for the inlet, outlet, and buffer ports. The flow channel was cut out of a 200  $\mu\text{m}$  thin double-sided polyimide tape and sandwiched between the bottom and top substrates. The width of the channel was 10 mm. An array of 16 NdFeB magnets was placed at the bottom of the chip to produce magnetic field within the channel. The permanent magnets were grade 52 block NdFeB magnets and were purchased from K&J Magnetics, Inc. (Pipersville, PA).

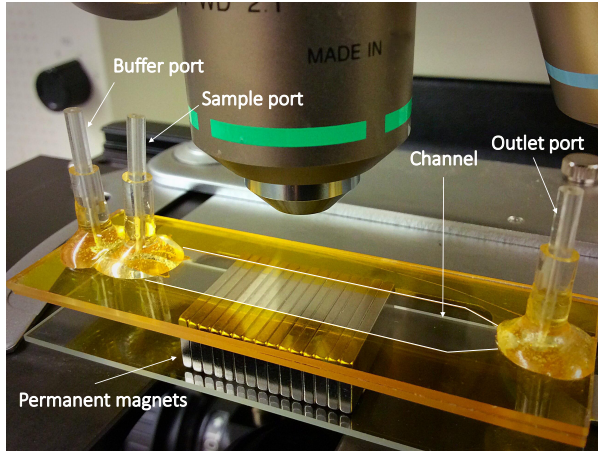


**Fig. 2** An image of an assembled chip.

## 4 Simulation results

### 4.1 Geometry and Boundary Conditions

A no-slip boundary condition was applied at the walls. At the inlet of the channel, a Dirichlet boundary condition with a constant velocity was applied to the channel inlet. The pressure at the outlet of the channel was uniform and equal to zero. For the permanent magnets, a relative permeability of 1.05 and a normal value of  $B_r = 1.43$  T for the remanence field were used. The initial velocities of the particles at the inlet of the channel were assumed to be equal to the corresponding fluid velocity at that point. Since the aspect ratio of fluidic channel (the ratio of the channel height to its width) is very small ( $\approx 1:50$ ), a symmetry boundary condition was applied to the symmetry planes located at  $z = 0$  and  $z = 0.02$  m.

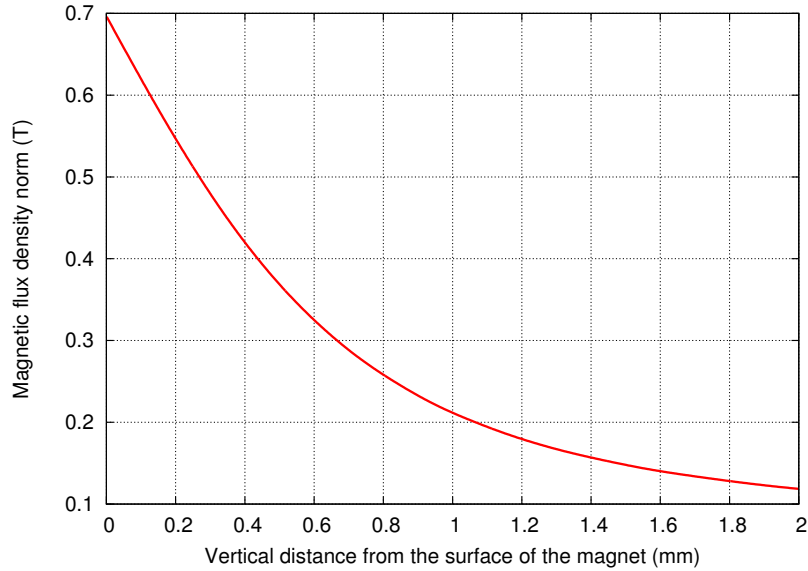
### 4.2 Magnetic field distribution

Magnetic field was simulated using the open-source software OpenFOAM for an array of magnets with opposing poles and the results were then used to study the behavior of particles motion in the presence of the magnetic field. The overall dimensions of the permanent magnets used in this study were  $19\text{ mm} \times 1.6\text{ mm} \times 6.35\text{ mm}$  ( $3/4'' \times 1/16'' \times 1/4''$ ). The magnets are magnetized through the 6.35 mm dimension.

#### 4.2.1 Modeling of a Single Magnet

A 3-D model of a single block magnet was created in OpenFOAM software. For NdFeB N52 grade magnets, a relative permeability of 1.05 and a normal value of  $B_r = 1.43$  T for the remanence field were used (Campbell 1996). Figure 3 shows the variation of the magnetic flux density as a function of the distance from the

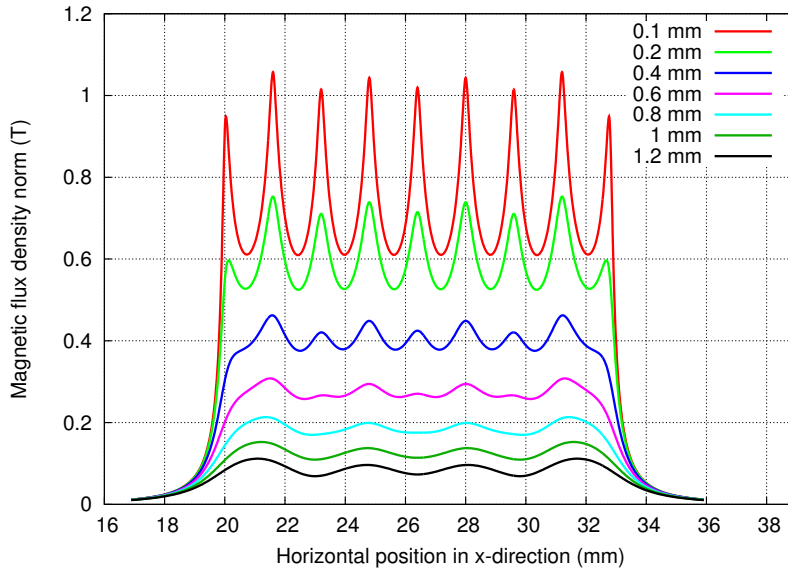
surface of the magnet. As can be seen from this figure, the magnetic flux density is approximately 0.7 T at the surface of the magnet and decreases nonlinearly as the distance from the surface of the magnet increases.



**Fig. 3** Magnetic flux density as a function of distance from the surface of a single magnet.

#### 4.2.2 Modeling an Array of Magnets

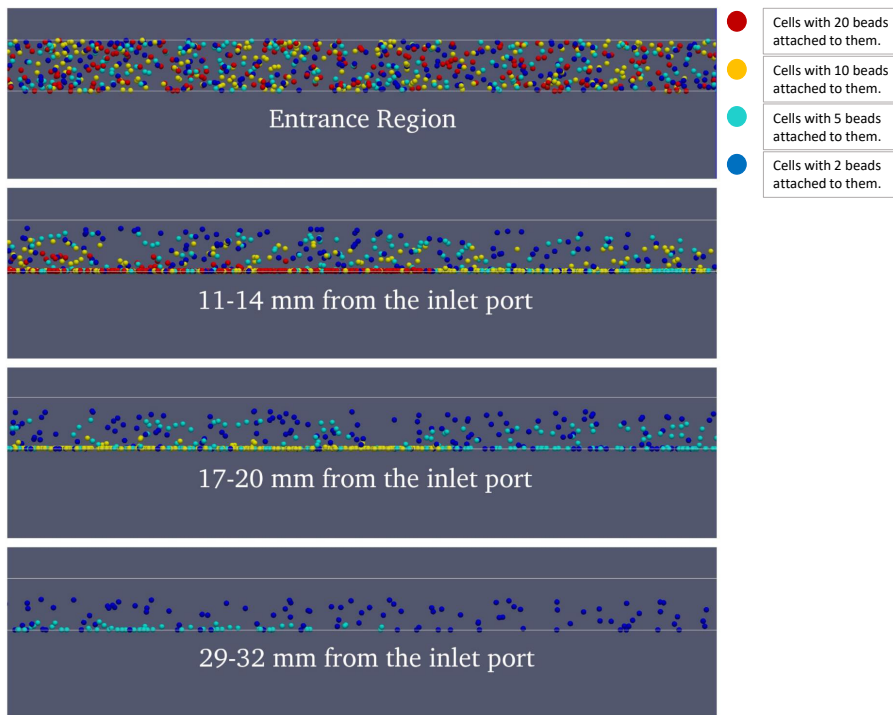
To investigate the effect of an array of magnets on the magnetic field distribution, the number of magnets was varied from 2 to 16. A repeatable magnetic field pattern at the interface of the magnets was observed when more than eight magnets was used. Figure 4 shows the distribution of the magnetic field for an array of 8 magnets. As can be seen from this figure, the magnetic flux density is nearly the same at the surface of each magnet and reaches its maximum value at the interface of the magnets, which is due to the alternating polarity arrangement (first magnet has north facing up, second magnet has south facing up, third magnet has north facing up, etc.). Therefore, the magnetic field along the channel has a repeating pattern between two peaks. Also, as the distance from the surface of the magnets increases, the peak values of the magnetic field decreases. A comparison between Figs. 3 and 4 clearly indicates that when an array of magnets with opposing poles is used, the magnetic flux density increases significantly at the interface of the magnets due to the alternating polarity arrangement.



**Fig. 4** Normal magnetic flux density distribution for an array of 8 magnets at various distances from the surface of the magnets.

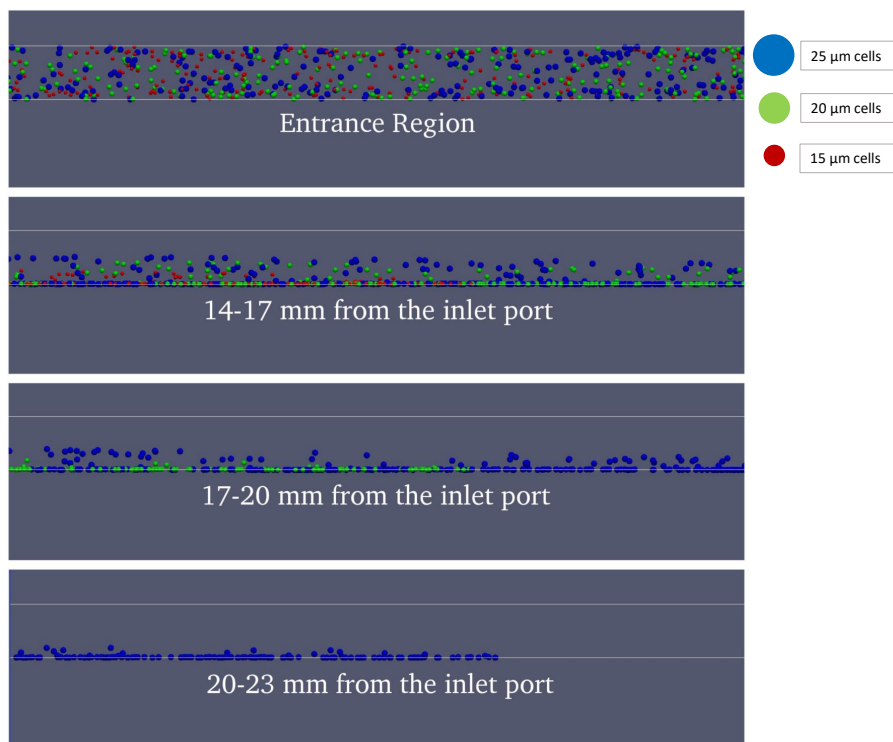
#### 4.3 Separation process modeling

Figure 5 is a demonstration of a two-dimensional cell separation process for a case where  $20 \mu\text{m}$  cells with different number of beads attached to them are injected into the separation channel. Red, yellow, light blue, and dark blue cells are tagged with 20, 10, 5, and 2 beads, respectively. The bead size and flow rate were  $1 \mu\text{m}$  and 100 ml/h. The saturation magnetization, magnetic susceptibility, and density of the beads are  $24 \text{ (Am}^2/\text{kg)}$ ,  $8 \times 10^{-4} \text{ (m}^3/\text{kg)}$ , and  $1700 \text{ (kg/m}^3)$ , respectively. The top, middle, and bottom windows demonstrate the snap shot images of different regions along the channel. The first window shows the entrance region which is free of magnets and the particles flow through this region without any deflection. Separation of the particles starts as soon as the particles experience the magnetic force. As the particles flow through the separation channel, they are gradually pulled down towards the magnets and are immobilized on the magnetic surfaces. The second window represents the channel above the 3rd and 4th magnets (11-14 mm from the inlet port). Red particles with 20 beads attached to them are separated within this region. As the number of beads decreases, the particles travel a longer distance before being captured. Yellow particles with 10 beads attached to them, are isolated within the 7th and 8th magnets (17-20 mm from the inlet port). For this particular case, 15 magnets are required to capture light blue cells with five beads attached to them (third window, 29-32 mm from the inlet port). Finally, the dark blue particles with 2 beads attached to them do not get captured and flow out of the separation channel.



**Fig. 5** Particle trajectories for  $20\ \mu\text{m}$  cells with different number of beads attached to them. Red, yellow, light blue, and dark blue cells are tagged with 20, 10, 5, and 2 beads, respectively. The bead size and flow rate were  $1\ \mu\text{m}$  and  $100\ \text{ml/h}$ .

Figure 6 represents a two-dimensional cell separation process for a case where cells with different sizes are injected into the separation channel. The diameter of red, green, and blue cells are  $15\ \mu\text{m}$ ,  $20\ \mu\text{m}$ , and  $25\ \mu\text{m}$ , respectively. Similar to the previous case, different windows demonstrate different regions within the channel. Initially, the particles travel through the entrance region without any deflection in their trajectory. Smaller particles experience smaller drag force compared to larger particles, as a result, smaller particles are expected to get captured faster. Second window shows the separation of  $15\ \mu\text{m}$  diameter red particles inside the channel above the 5th and 6th magnets (14-17 mm from the inlet port). 8 magnets are required to fully separate the green particles with particle size of  $20\ \mu\text{m}$  (17-20 mm from the inlet port). Finally, the largest particles with the diameter of  $25\ \mu\text{m}$  are separated within 10 magnets (20-23 mm from the inlet port).



**Fig. 6** Particle trajectories for cells with different diameters. The diameter of red, green, and blue cells are  $15\ \mu\text{m}$ ,  $20\ \mu\text{m}$ , and  $25\ \mu\text{m}$ , respectively. The number of beads, bead size, and flow rate were 10,  $1\ \mu\text{m}$ , and  $100\ \text{mL/h}$ .

## 5 Experimental setup

To verify and validate the simulation results, a series of tests were conducted using magnetic beads and the trajectories of the beads within the channel were monitored and recorded. Since it was impossible to observe and capture images from the side-view of the channel, efforts were made to come up with a chip design that enables us to monitor and observe the trajectories of the magnetic beads from the top under an optical microscope. The design of the chip was such that the magnets were placed at the edge of the chip and the distance between the channel and the magnets was  $1\ \text{mm}$ . This arrangement is similar to the chip design used in the simulations where the channel height was  $200\ \mu\text{m}$  and the magnets were placed on the bottom of the chip,  $1\ \text{mm}$  away from the channel. The average velocity was kept at  $13.9\ \text{mm/s}$ . At this velocity, the equivalent flow rate in a chip with a channel width of  $10\ \text{mm}$  and a channel height of  $200\ \mu\text{m}$  (same dimensions used in the simulations) would be  $100\ \text{mL/h}$ . Figure 7(a) shows a CAD drawing of the microfluidic pattern which allows viewing the particles from the top by placing the magnets at the edge of the chip. A photograph of an assembled chip is shown in Fig. 7(b). To perform experiments, a 1:100 dilution sample was prepared by mixing  $10\ \mu\text{L}$  magnetic beads with  $990\ \mu\text{L}$  deionized water under

gentle shaking. The diameter of the magnetic beads was  $1\ \mu\text{m}$ . Before introducing the sample into the channel, the chip and tubing were washed with deionized water and soaked with 20 % bovine serum albumin (BSA) for 30 minutes and rinsed with an isolation buffer. Next, 1 mL of the diluted bead sample was injected into the separation channel using a bidirectional milliGAT pump. The trajectories of the beads were observed under an optical microscope and captured at various sections of the chip along the channel.

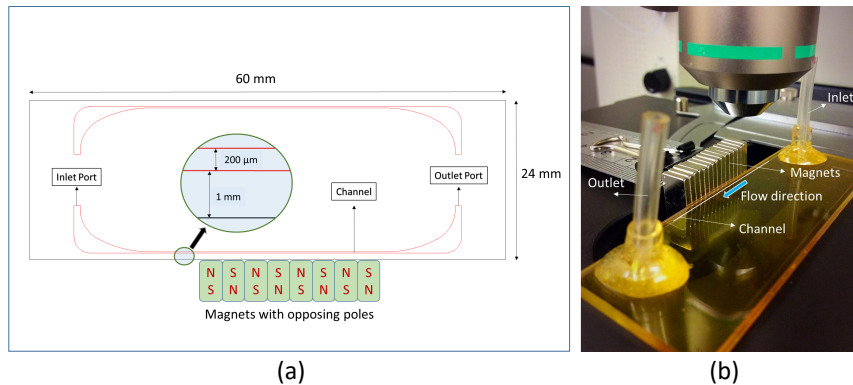


**Fig. 7** (a) A CAD drawing of the microfluidic channel. (b) A fabricated glass based microfluidic device.

## 6 Experimental results

Figure 8 displays a comparison between the experimental and simulation results for  $1\ \mu\text{m}$  magnetic beads at an average fluid velocity of  $13.9\ \text{mm/s}$ . The channel height is  $200\ \mu\text{m}$  and the length of each frame is  $400\ \mu\text{m}$  which is approximately equal to  $1/4$  of a magnet. Efforts were made to ensure a close approximation between the model and the actual bead separation experiments. 10,000 magnetic beads were injected into the channel and their trajectories were observed under an optical microscope. In the absence of magnetic fields, particles are uniformly spread across the entrance region of the channel and move with fluid in the x-direction. This is evidenced by the experimental image in window a, and the simulated particle trajectories in window a'. When the magnetic particles approach the magnets, they are deflected towards the bottom of the channel due to the downward magnetic force, resulting in a particle-free region near the upper wall of the channel. Window b depicts a region above the first magnet which indicates that the magnetic beads are confined within approximately the bottom  $2/3$  of the channel. This observation is consistent with the predicted particle trajectories as shown in frame b'. Frames c and d demonstrate the particle trajectories above the 2nd the 3rd magnets, respectively. The results indicate that the magnetic beads are further pulled down

and confined within the bottom  $1/2$  and  $1/3$  of the channel. Also, as can be seen from these images the experimental and simulation results are in good agreement.

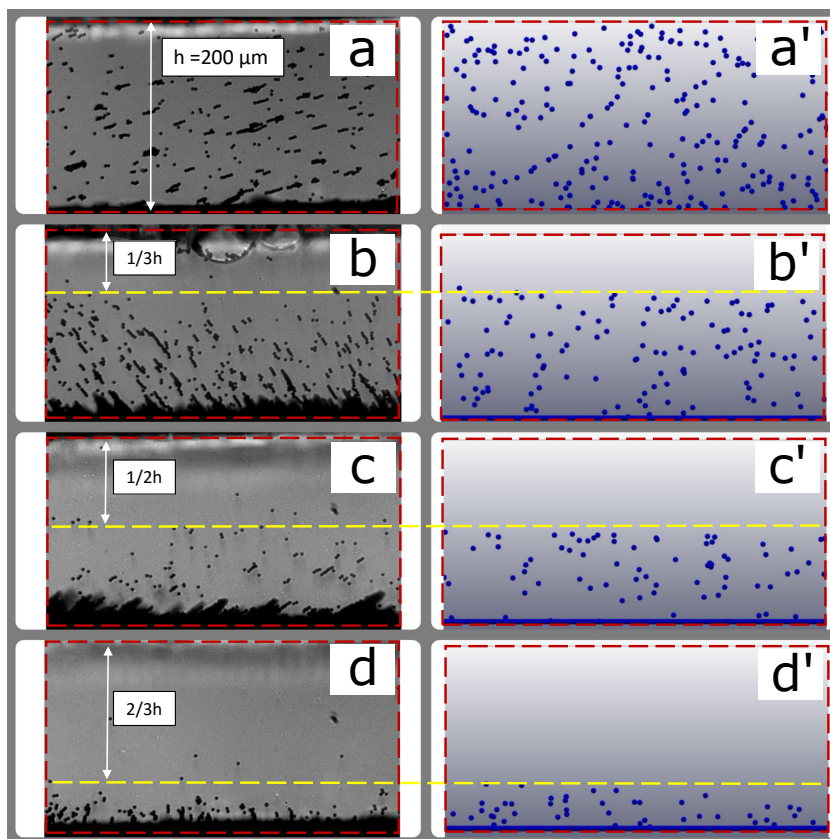


**Fig. 8** A comparison between the experimental and simulation results for the deflection of  $1 \mu\text{m}$  magnetic beads at an average fluid velocity of  $13.9 \text{ mm/s}$ . Left images show micrographs of experimental observations while the right figures show the simulated trajectories. Panels a and a': Entrance Region. Panels b and b': First Magnet. Panels c and c': Second Magnet. Panels d and d': Third Magnet.

## 7 Parametric study

To improve the performance of the separation device, a parametric study was performed to investigate the effects of the number of beads per cell, cell size, flow rate, and magnetic bead size on the cell separation performance. For all cases, the height of the channel and the thickness of the substrate were kept constant at  $200 \mu\text{m}$  and  $1 \text{ mm}$ , respectively. Other parameters such as number of beads, cell size, flow rate, and bead size were varied. The location of the first magnet is represented by a dashed line at  $x = 7 \text{ mm}$  in Figs. 9 to 12.

Figure 9 shows the particle trajectory for different number of beads attached to each cell. The cell size and bead size were  $20 \mu\text{m}$  and  $1 \mu\text{m}$ , respectively. The

flow rate was 100 ml/h which corresponds to the average velocity of 13.9 mm/s within the channel. The results indicate that the trapping length decreases as the number of beads increases. This is because the magnetic force is proportional to the number of beads, and as the number of beads increases, the magnetic force increases as well. The results also show that for the cell size of 20  $\mu\text{m}$  and the flow rate of 100 ml/h, at least 5 magnetic beads are required to capture the cells.

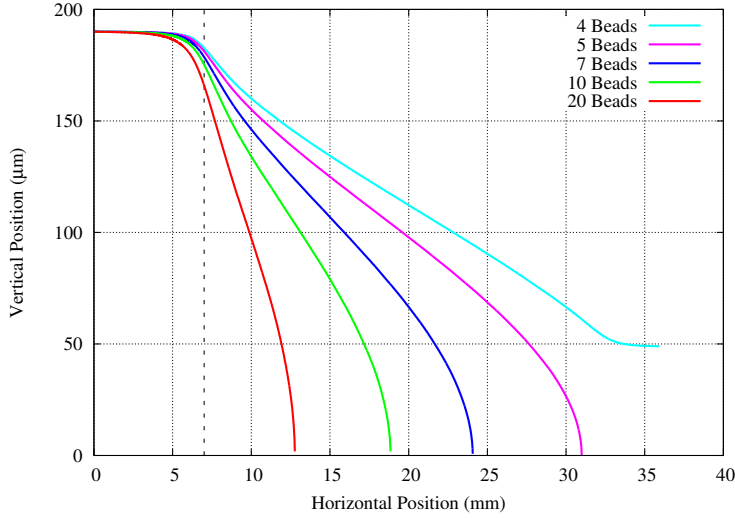


**Fig. 9** Particle trapping for different number of beads per cell. The cell size, bead size, and flow rate were 20  $\mu\text{m}$ , 1  $\mu\text{m}$ , and 100 ml/h.

The correct number of beads that are required to separate cells depends on the average cell size. Red blood cells can vary in size due to pathologies but they are mostly 7.5-8  $\mu\text{m}$  in diameter. The average size of a white blood cell is around 10  $\mu\text{m}$  in diameter and circulating tumor cells appear to have a diameter between 12  $\mu\text{m}$  and 25  $\mu\text{m}$ .

Figure 10 shows the particle trajectory for cell sizes of 10  $\mu\text{m}$ , 15  $\mu\text{m}$ , 20  $\mu\text{m}$ , 25  $\mu\text{m}$ , and 30  $\mu\text{m}$ . Depending on the cell size, the average number of beads attached to each cell can vary, however, here the number of beads was assumed to remain constant and equal to 10 in all cases. The results show that for the flow rate of 100 mL/h, the capture length increases as the size of the cell increases. This is due to the fact that, the drag force is proportional to the cell size, and as the cell size increases, the drag force increases. Thus, for a constant magnetic force, the capture length increases with increasing the cell size.

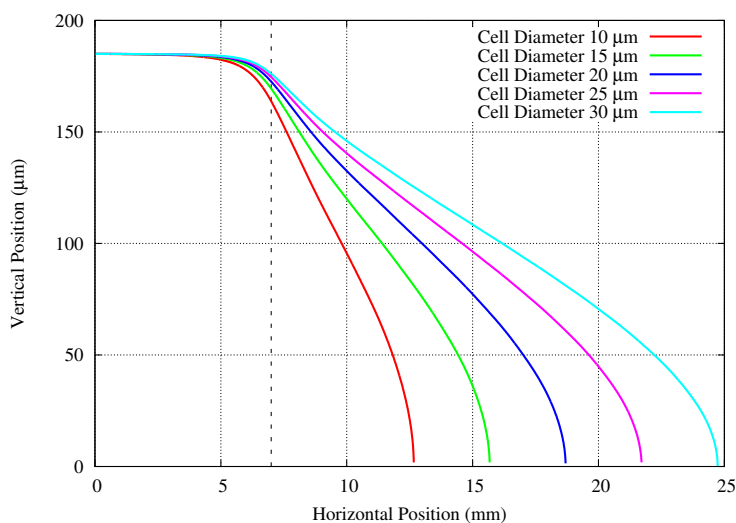


**Fig. 10** Particle trapping for cells with different sizes. The number of beads, bead size, and flow rate were 10 , 1  $\mu m$ , and 100 mL/h.

Separation of small micro particles at different flow rates highly depends on the magnitude of the magnetic force inside the channel. For larger magnetic forces, higher input flow rates can be used to inject the particle-fluid solution inside the channel. As shown in Figure 11, the capture length increases as the flow rate increases. This is because the particle velocity along the channel increases with increasing the flow rate, resulting in a larger capture length. The results also show that as the flow rate exceeds 250 mL/h, depending on the position of the particle inside the channel, some of the particles do not get captured and exit the channel.

Magnetic beads come in several sizes for use in a wide variety of applications. Dynabeads are available in three different diameter sizes - 1  $\mu m$ , 2.8  $\mu m$ , and 4.5  $\mu m$ . Figure 12 shows the effect of different bead size on the particle trajectory. The number of beads, cell size, and flow rate were 1, 20  $\mu m$ , and 100 mL/h, respectively. As can be seen, the capture length decreases as the bead size increases. This is due to the fact that the magnetic force is proportional to the cube of the diameter of the bead, Eq. (3), and as the bead size increases from 1  $\mu m$  to 2.8 and 4.5  $\mu m$ , the magnetic force increases by a factor of 20 and 90 times, respectively, resulting in a shorter capture length. The results show that the particles tagged with 2.8 and 4.5  $\mu m$  beads are captured within 5 mm and 1 mm from the first magnet, respectively, while a 1  $\mu m$  bead size is not sufficient to trap the particles.

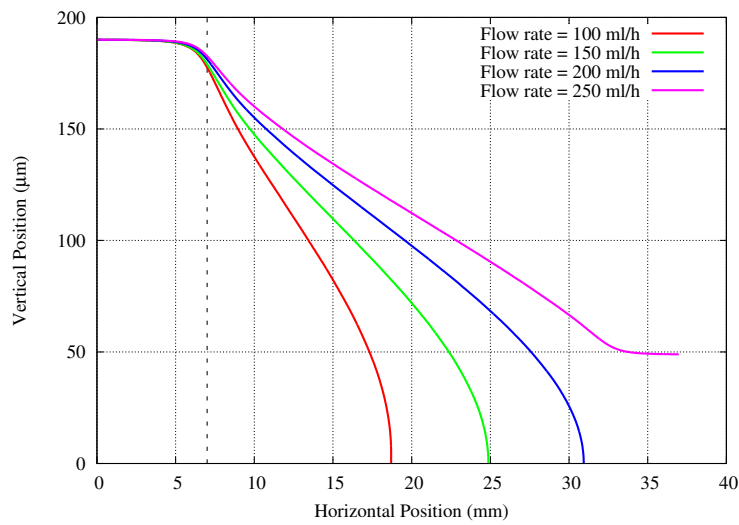


**Fig. 11** Particle trapping for different flow rates. The number of beads, cell size, and bead size were 10, 20  $\mu\text{m}$ , 1  $\mu\text{m}$ .

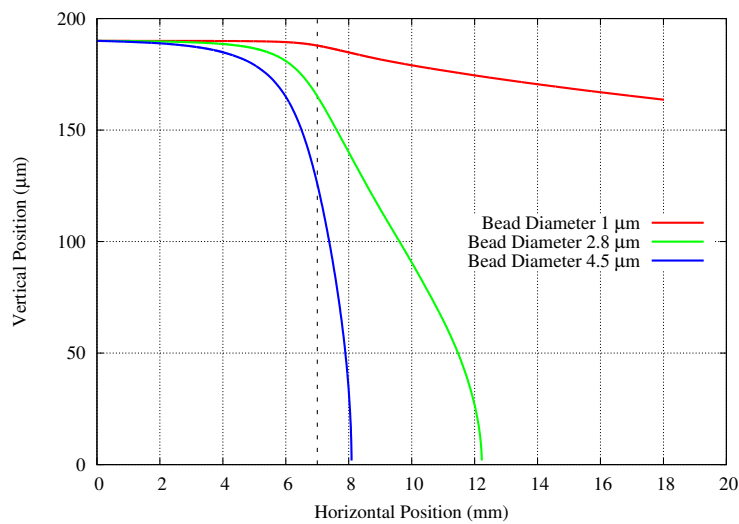


**Fig. 12** Particle trapping for cells with different bead size attached to them. The number of beads, cell size, and flow rate were 1, 20  $\mu\text{m}$ , and 100 mL/h.

## 8 Conclusions

In summary, trajectories and capture of bioparticles were successfully simulated in a magnetophoretic bio-separation chip. It was shown that, due to the alternating polarity arrangement of the magnets, large magnetic fields gradients were produced inside the channel. Simulations were performed to predict the trajectories

---

and capture length of the particles within the separation channel. The numerical simulation results were verified by conducting an experiment, where the deflection of  $1\ \mu\text{m}$  magnetic beads at an average fluid velocity of  $13.9\ \text{mm/s}$  inside the separation channel was studied. A good qualitative agreement between the experimental and numerical results was obtained. Finally, A comprehensive parametric study was performed, which indicated that the trapping length decreases with increasing the number of beads per cell and the bead size. However, the trapping length increases as the size of the cell increases. The size of the beads greatly influenced the capture efficiency. As the bead size increases from  $1\ \mu\text{m}$  to  $2.8$  and  $4.5\ \mu\text{m}$ , the magnetic force increases by a factor of 20 and 90 times, respectively, allowing the chip to operate at higher sample flow rates.

**Acknowledgements** This work was partially supported by an RGGS grant from the SIUE Graduate School.

## References

- Adams, J. D., Kim, U., and Soh, H. T. (2008). Multitarget magnetic activated cell sorter. *Proceedings of the National Academy of Sciences*, 105(47):18165–18170.
- Arruebo, M., Fernández-Pacheco, R., Ibarra, M. R., and Santamaría, J. (2007). Magnetic nanoparticles for drug delivery. *Nano today*, 2(3):22–32.
- Bleaney, B. I. and Bleaney, B. (1989). *Electricity and Magnetism*. Oxford University Press.
- Campbell, P. (1996). *Permanent magnet materials and their application*. Cambridge University Press.
- Chen, Y., Li, P., Huang, P.-H., Xie, Y., Mai, J. D., Wang, L., Nguyen, N.-T., and Huang, T. J. (2014). Rare cell isolation and analysis in microfluidics. *Lab on a Chip*, 14(4):626–645.
- Cho, S. H., Godin, J. M., Chen, C.-H., Qiao, W., Lee, H., and Lo, Y.-H. (2010). Review article: Recent advancements in optofluidic flow cytometer. *Biomicrofluidics*, 4(4):043001.
- Darabi, J. and Guo, C. (2013). On-chip magnetophoretic isolation of CD4+ T cells from blood. *Biomicrofluidics*, 7(5):054106.
- Darabi, J. and Guo, C. (2016). Continuous isolation of monocytes using a magnetophoretic-based microfluidic chip. *Biomedical microdevices*, 18(5):77.
- Derec, C., Wilhelm, C., Servais, J., and Bacri, J.-C. (2010). Local control of magnetic objects in microfluidic channels. *Microfluidics and Nanofluidics*, 8(1):123–130.
- Di Carlo, D. (2009). Inertial microfluidics. *Lab on a Chip*, 9(21):3038–3046.
- Earhart, C. M., Hughes, C. E., Gaster, R. S., Ooi, C. C., Wilson, R. J., Zhou, L. Y., Humke, E. W., Xu, L., Wong, D. J., Willingham, S. B., et al. (2014). Isolation and mutational analysis of circulating tumor cells from lung cancer patients with magnetic sifters and biochips. *Lab on a Chip*, 14(1):78–88.
- Forbes, T. P. and Forry, S. P. (2012). Microfluidic magnetophoretic separations of immunomagnetically labeled rare mammalian cells. *Lab on a Chip*, 12(8):1471–1479.
- Furlani, E. (2006). Analysis of particle transport in a magnetophoretic microsystem. *Journal of Applied Physics*, 99(2):024912.
- Furlani, E. (2007). Magnetophoretic separation of blood cells at the microscale. *Journal of Physics D: Applied Physics*, 40(5):1313.
- Häfel, U., Schütt, W., Teller, J., and Zborowski, M. (2013). *Scientific and clinical applications of magnetic carriers*. Springer Science & Business Media.
- Hale, C. and Darabi, J. (2014). Magnetophoretic-based microfluidic device for DNA isolation. *Biomicrofluidics*, 8(4):044118.
- Han, K.-H., Han, A., and Frazier, A. B. (2006). Microsystems for isolation and electrophysiological analysis of breast cancer cells from blood. *Biosensors and bioelectronics*, 21(10):1907–1914.
- Hoshino, K., Huang, Y.-Y., Lane, N., Huebschman, M., Uhr, J. W., Frenkel, E. P., and Zhang, X. (2011). Microchip-based immunomagnetic detection of circulating tumor cells. *Lab on a Chip*, 11(20):3449–3457.

- Inglis, D. W., Riehn, R., Austin, R., and Sturm, J. (2004). Continuous microfluidic immunomagnetic cell separation. *Applied Physics Letters*, 85(21):5093–5095.
- Jackson, J. D. (1999). *Classical Electrodynamics*. John Wiley & Sons.
- Jung, J. and Han, K.-H. (2008). Lateral-driven continuous magnetophoretic separation of blood cells. *Applied Physics Letters*, 93(22):223902.
- Jung, Y., Choi, Y., Han, K.-H., and Frazier, A. B. (2010). Six-stage cascade paramagnetic mode magnetophoretic separation system for human blood samples. *Biomedical microdevices*, 12(4):637–645.
- Kashevsky, S. and Kashevsky, B. (2013). Analytical model of batch magnetophoretic separation. *Physical Review E*, 87(6):062308.
- Kayani, A. A., Khoshmanesh, K., Ward, S. A., Mitchell, A., and Kalantar-Zadeh, K. (2012). Optofluidics incorporating actively controlled micro-and nanoparticles. *Biomicrofluidics*, 6(3):031501.
- Khashan, S., Alazzam, A., and Furlani, E. (2014). Computational analysis of enhanced magnetic bioseparation in microfluidic systems with flow-invasive magnetic elements. *Scientific reports*, 4.
- Khashan, S. A. and Furlani, E. P. (2012). Effects of particle–fluid coupling on particle transport and capture in a magnetophoretic microsystem. *Microfluidics and nanofluidics*, 12(1-4):565–580.
- Laurell, T., Petersson, F., and Nilsson, A. (2007). Chip integrated strategies for acoustic separation and manipulation of cells and particles. *Chemical Society Reviews*, 36(3):492–506.
- Lee, H., Jung, J., Han, S.-I., and Han, K.-H. (2010). High-speed RNA microextraction technology using magnetic oligo-dT beads and lateral magnetophoresis. *Lab on a Chip*, 10(20):2764–2770.
- Liang, L., Zhang, C., and Xuan, X. (2013). Enhanced separation of magnetic and diamagnetic particles in a dilute ferrofluid. *Applied Physics Letters*, 102(23):234101.
- Lin, S.-C. S., Mao, X., and Huang, T. J. (2012). Surface acoustic wave (SAW) acoustophoresis: now and beyond. *Lab on a chip*, 12(16):2766–2770.
- Liu, C., Lagae, L., Wirix-Speetjens, R., and Borghs, G. (2007). On-chip separation of magnetic particles with different magnetophoretic mobilities. *Journal of applied physics*, 101(2):024913.
- Pamme, N. (2012). On-chip bioanalysis with magnetic particles. *Current opinion in chemical biology*, 16(3):436–443.
- Pamme, N. and Wilhelm, C. (2006). Continuous sorting of magnetic cells via on-chip free-flow magnetophoresis. *Lab on a Chip*, 6(8):974–980.
- Pethig, R. (2010). Review article dielectrophoresis: status of the theory, technology, and applications. *Biomicrofluidics*, 4(2):022811.
- Plouffe, B. D., Mahalanabis, M., Lewis, L. H., Klapperich, C. M., and Murthy, S. K. (2012). Clinically relevant microfluidic magnetophoretic isolation of rare-cell populations for diagnostic and therapeutic monitoring applications. *Analytical chemistry*, 84(3):1336–1344.
- Purcell, E. M. and Morin, D. J. (2013). *Electricity and magnetism*. Cambridge University Press.
- Regtmeier, J., Eichhorn, R., Viefhues, M., Bogunovic, L., and Anselmetti, D. (2011). Electrodeless dielectrophoresis for bioanalysis: theory, devices and applications. *Electrophoresis*, 32(17):2253–2273.

- 
- Shen, F., Hwang, H., Hahn, Y. K., and Park, J.-K. (2012). Label-free cell separation using a tunable magnetophoretic repulsion force. *Analytical chemistry*, 84(7):3075–3081.
- Tsutsui, H. and Ho, C.-M. (2009). Cell separation by non-inertial force fields in microfluidic systems. *Mechanics research communications*, 36(1):92–103.
- Verbarg, J., Kamgar-Parsi, K., Shields, A. R., Howell, P. B., and Ligler, F. S. (2012). Spinning magnetic trap for automated microfluidic assay systems. *Lab on a chip*, 12(10):1793–1799.
- Xia, N., Hunt, T. P., Mayers, B. T., Alsberg, E., Whitesides, G. M., Westervelt, R. M., and Ingber, D. E. (2006). Combined microfluidic-micromagnetic separation of living cells in continuous flow. *Biomedical Microdevices*, 8(4):299–308.
- Zeng, J., Deng, Y., Vedantam, P., Tzeng, T.-R., and Xuan, X. (2013). Magnetic separation of particles and cells in ferrofluid flow through a straight microchannel using two offset magnets. *Journal of Magnetism and Magnetic Materials*, 346:118–123.